Polyamide-imide Nanofiltration Hollow Fiber Membranes with Elongation-Induced Nano-Pore Evolution

Shi Peng Sun
Singapore-MIT Alliance, National University of Singapore, Singapore 119260; and
Dept. of Chemical & Biomolecular Engineering, National University of Singapore, Singapore 119260

Kai Yu Wang and D. Rajarathnam
Dept. of Chemical & Biomolecular Engineering, National University of Singapore, Singapore 119260

T. Alan Hatton
Singapore-MIT Alliance, National University of Singapore, Singapore 119260; and
Dept. of Chemical Engineering, Massachusetts Institute of Technology, Cambridge, MA 02139

Tai-Shung Chung
Singapore-MIT Alliance, National University of Singapore, Singapore 119260; and
Dept. of Chemical & Biomolecular Engineering, National University of Singapore, Singapore 119260

DOI 10.1002/aic.12083

The molecular design of nanoporous membranes with desired morphology and selectivity has attracted significant interest over the past few decades. A major problem in their applications is the trade-off between sieving property and permeability. Here, we report the discovery of elongation-induced nano-pore evolution during the external stretching of a novel polyamide-imide nanofiltration hollow fiber membrane in a dry-jet wet-spinning process that simultaneously leads to a decreased pore size but increased pure water permeability. The molecular weight cutoff, pore size, and pore size distribution were finely tuned using this approach. AFM and polarized FTIR verified the nano-pore morphological evolution and an enhanced molecular orientation in the surface skin layer. The resultant nanofiltration membranes exhibit highly effective fractionation of the monovalent and divalent ions of NaCl/Na_2SO_4 binary salt solutions. More than 99.5% glutathione can be rejected by the nanofiltration membranes at neutral pH, offering the feasibility of recovering this tripeptide. © 2009 American Institute of Chemical Engineers *AIChE J,* 56: 1481–1494, 2010

Keywords: hollow fiber membranes, nanofiltration, polyamide-imide (PAI), Torlon®, glutathione

Introduction

Since its inception in the early 1970s, nanofiltration (NF) has grown rapidly and become very important for liquid based separation processes through its unique ability to

---

Additional Supporting Information may be found in the online version of this article.

Correspondence concerning this article should be addressed to T.-S. Chung at chencts@nus.edu.sgT.-S. Chung at chencts@nus.edu.sg.

separate and fractionate ionic and low molecular weight organic species.[1] NF is one of a class of pressure-driven membrane separation processes, with a nominal molecular weight cutoff (MWCO; molecular weight of solute that is 90% rejected by the membrane) ranging from 200 to 1000 Dalton and pore sizes of about 0.5–2.0 nm.[2] It offers advantages of higher retention than ultrafiltration (UF) and lower pressure requirement than reverse osmosis (RO).[3] The major separation mechanisms of NF involve a steric (size exclusion) effect and an electrostatic partitioning interaction (Donnan exclusion) between the membrane and an external solution.[4] Therefore, NF has become a promising separation and purification method in water treatment,[5,6] and in the chemical,[7] pharmaceutical,[8,9] petrochemical,[10] and other industries.

Most conventional NF membranes are made of thin film composites (TFC). Generally, these membranes consist of a thick, porous, nonselective support layer covered by an ultrathin barrier layer, which is prepared by interfacial polymerization, coating or chemical modification.[11] The several sophisticated steps involved in the fabrication process render it time consuming and cost ineffective. Moreover, most NF modules are still made in the spiral-wound configuration by using flat-sheet membranes wound around a central tube. Compared to flat-sheet membranes, hollow fibers have the following advantages: (1) a much larger membrane area per unit membrane module volume, resulting in a higher productivity; (2) self-mechanical support, allowing the membrane to be back-flushed for liquid separation; and (3) good flexibility and ease of handling during module fabrication and system operation. Nevertheless, the applications of hollow fiber membranes are still limited due to their low water permeability relative to that of flat-sheets primarily because they are usually spun from dopes containing much higher concentrations than those used for the fabrication of flat sheet membranes to maintain self-supported mechanical strength and withstand high testing pressures.[12] In addition, the high shear rates and stresses during the spinning process generally enhance chain orientation, and thus, produce lower water permeability and higher solute rejection.[13] Clearly, technological breakthroughs are needed to enhance the water permeability of hollow fiber membranes while still retaining their separation efficiency. The objective of this study is, therefore, to explore the molecular engineering and characterization of NF hollow fiber membranes with the desired water permeability and pore size distribution. We accomplish these tasks by controlling the elongation-induced membrane pore morphology by external stretching of the fibers during the spinning process.

Molecular engineering of pore size and chain orientation in polymeric membranes has been used effectively to control the transport properties of both gases and liquids.[14] Several researchers have investigated shear-induced molecular orientation and its effects on the performance of gas separation[15–17] and UF[18,19] hollow fiber membranes. However, much less work has been done on the elongation-induced morphological evolution during the preparation of NF hollow fiber membranes. Wang and Chung first observed an interesting consequence of elongation-induced nano-pore formation during the fabrication of a novel polybenzimidazole (PBI) NF hollow fiber membrane[20]; the effective mean pore size decreased whereas the pure water permeability (PWP) increased with an increase in the elongational draw ratio. This phenomenon is quite different from that reported on the effects of elongational draw ratio on UF membranes and gas separation membranes,[15–19] and these observations stimulated our interest in further investigating elongation-induced nanopore evolution in other NF membranes. To the best of our knowledge, no in-depth studies on this subject have yet been reported. Because the hollow fiber configuration is the preferred choice for industrial membrane systems and the use of high take-up speeds is favorable in the spinning process,[12,21,22] this study may have great potential in developing tailor-made high-performance NF membranes for various industrial applications.

In this study, Torlon® 4000TF polyamide-imide (PAI), as shown in Figure 1,[23] was adopted as the membrane material because it has both superior mechanical properties typically associated with polyamides, and high thermal stability and solvent resistance associated with polyimides.[24] Torlon® has been used widely in the injection molding of engine parts for racing cars, of molded parts for the space shuttle, and of many other critical components. Only recently has Torlon® been applied in the membrane field, in areas such as vapor permeation,[25] pervaporation,[24,26,27] and gas separation.[28–30] Although Torlon® has also been utilized to fabricate NF membranes, it has only served as the supporting layer in flat-sheet membranes.[31] The uniqueness of our work is in that wholly integral Torlon® PAI NF membranes are fabricated from a polymer/solvent binary system in the absence of additives by a one-step phase-inversion process without further modification.

In addition to the molecular engineering of Torlon® PAI NF hollow fiber membranes and the fundamentals of elongation-induced nano-pore evolution, we also investigate the newly developed NF hollow fiber membranes for ion fractionation and the separation of glutathione from aqueous solutions. Glutathione (L-γ-glutamyl-L-cysteinylglycine), a tripeptide, is the most abundant low-molecular-weight thiol compound in living organisms. It has already been used widely as a therapeutic drug because of its multiple biological functions as an antioxidant, immunity booster, and detoxifier.[32] Currently, this tripeptide is produced by yeast fermentation, chemical and enzymatic methods.[33] Because the glutathione molecule contains the amino ($-NH_2$), carboxyl ($-COOH$), and thiol ($-SH$) groups, its ionization state varies with aqueous solution pH, as shown in Figure 2. On the basis of the interaction between ionized glutathione molecules and the negatively charged membrane, NF could become a promising candidate to recover, concentrate, and purify glutathione from aqueous solutions by adjusting pH values.[34]

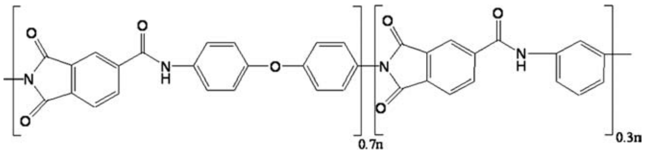

Figure 1. The general structure for Torlon® 4000T Poly (amide imide).[23]

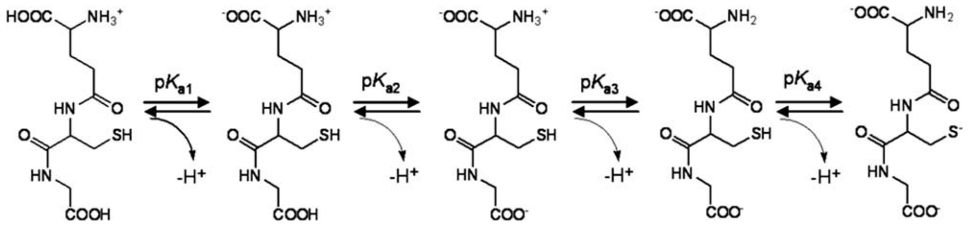

Figure 2. Ionization states of glutathione at different pH values.

pK_{a1} = 2.12, pK_{a2} = 3.59, pK_{a3} = 8.75, pK_{a4} = 9.65.

Theoretical Background

Determination of mean effective pore size, pore size distribution, and molecular weight cutoff

It has been found that the solute rejection R_T for synthetic membranes can be expressed by a log-normal probability function of solute size, as described in the following equation[35]:

$$R_T = 1 - \frac{c_p}{c_f} = \mathrm{erf}(y) = \frac{1}{\sqrt{2\pi}} \int_{-\infty}^{y} e^{-(u^2/2)} du \tag{1}$$

where c_f and c_p are the feed and permeate stream concentrations, respectively, $y = \frac{\ln r_s - \ln \mu_s}{\ln \sigma_g}$, r_s is the solute radius, μ_s is the geometric mean solute radius at R_T = 50%, and σ_g is the geometric standard deviation about μ_s, defined as the ratio of r_s at R_T = 84.13% to that at R_T = 50%. When the solute rejection of a membrane is plotted against solute radius on log-normal probability coordinates, a straight line is obtained:

$$F(R_T) = A + B(\ln r_s) \tag{2}$$

By ignoring the influence of steric and hydrodynamic interactions between the solute and the pores on the solute rejection, the mean effective pore radius (μ_p) and the geometric standard deviation (σ_p) can be assumed to be the same as μ_s and σ_g, respectively. Therefore, based on μ_p and σ_p, the pore size distribution of an NF membrane is given by the probability density function[36]:

$$\frac{dR_T(r_p)}{dr_p} = \frac{1}{r_p \ln \sigma_p \sqrt{2\pi}} \exp\left[-\frac{(\ln r_p - \ln \mu_p)^2}{2(\ln \sigma_p)^2}\right] \tag{3}$$

where r_p is the effective pore radius of the membrane. The values of μ_p and σ_p determine the position and sharpness of the distribution curves, respectively.

In this study, different solutions containing single neutral solutes were used to measure the solute rejection (R_T) by relying on the relationship between Stokes radius r_s and molecular weight, MW of these known neutral solutes, which can be expressed by the following equation[37]:

$$\log r_s = -1.32 + 0.395 \log \mathrm{MW} \tag{4}$$

with units of nm for r_s and g/mol for MW. From this equation, the radius of a hypothetical solute at a given MW can be obtained. This equation can also be used back to calculate MW of an unknown solute at a given radius.

Determination of reflection coefficient σ, the solute permeability P*, and effective charge density* ΦX

Solute transport phenomena during the nanofiltration process can be described using irreversible thermodynamics. Kedem and Katchalsky[38] proposed the relation between the volumetric flux J_v and the solute flux J_s through a membrane to be

$$J_v = L_p(\Delta p - \sigma \Delta \pi) \tag{5}$$

$$L_s = (P/\delta)(c_f - c_p) + (1 - \sigma) J_v \bar{c} \tag{6}$$

Equations 5 and 6 indicate that transport across a membrane is characterized by four transport parameters, i.e., the PWP L_p, the reflection coefficient σ, and the intrinsic solute permeability P as well as the membrane thickness, δ.

When the concentration difference between the feed and the permeate is high, Spiegler and Kedem[39] improved this model to express it in a differential form as follows:

$$J_s = -P\left(\frac{dc}{dx}\right) + (1 - \sigma) J_v c \tag{7}$$

Integration of Eq. 7 across the membrane thickness yields the Spiegler-Kedem equation:

$$R_T = 1 - \frac{c_p}{c_f} = \frac{\sigma(1 - F)}{1 - \sigma F}, \tag{8}$$

where

$$F = \exp\left[-\left(\frac{1 - \sigma}{P/\delta}\right) J_v\right].$$

The Spiegler-Kedem equation is usually applied when there are no electrostatic interactions between the membrane and neutral solutes. From Eq. 8, one can see that the reflection coefficient σ corresponds to the maximum rejection at an infinitely high permeate volume flux. The values of σ and P/δ can be determined directly from experimental data on the real rejection R_T, as a function of J_v by any suitable regression method. Instead of the intrinsic permeability, P,

Table 1. Diffusivities and Stokes Radii of Neutral Solutes in Aqueous Solutions (at 25°C)[40]

Solute	MW (g/mol)	D_s ($\times 10^{-9}$ m^2/s)	r_s (nm)
Glucose	180	0.67	0.365
Saccharose	342	0.52	0.471
Raffinose	504	0.42	0.584
α-Cyclodextrin	972	0.35	0.701

the solute permeability, P/δ, which is defined by Spiegler and Kedem, is reported because the membrane thickness is difficult to measure accurately.

For monovalent electrolytes (e.g., NaCl), membrane parameters σ and P can be determined by combining the extended Nernst-Planck equation and the Donnan equilibrium theory, in accordance with the Teorell-Meyer-Sievers (TMS) model with the following results[40]:

$$\sigma = 1 - \frac{2}{(2\alpha - 1)\xi + (\xi^2 + 4)^{0.5}} \tag{9}$$

$$P = D_s(1 - \sigma)\varepsilon \tag{10}$$

where ξ is defined as the ratio of the fixed charge density (X) of the membrane to the electrolyte concentration (c_m) at the membrane surface, ε is the membrane porosity, α is the transport number of cations in free solution, defined as $\alpha = D_1/(D_1 + D_2)$, where D_1 and D_2, the diffusivities of Na^+ and Cl^-, are 1.33×10^{-9} and 2.03×10^{-9} m^2/s, respectively.[41] Because the fixed charge density varies with electrolyte concentration, the effective charge density, ΦX was introduced in the following empirical equation[40,42]:

$$\Phi X = K c_m^n \tag{11}$$

where K and n are constants. The effective charge density of a membrane can thus be determined as a function of NaCl concentration if σ and α are available.

Experimental

Materials

Torlon® 4000TF polyamide-imide with the chemical structure shown in Figure 1 was purchased from Solvay Advanced Polymers. *N*-methyl-2-pyrrolidinone (NMP) was purchased from Merck and used as the solvent for the spinning solution. Uncharged neutral solutes of glucose, saccharose, raffinose, and α-cyclodextrin (Sigma-Aldrich) were utilized to characterize membrane structure parameters. Molecular weights, diffusivities, and Stokes radii of neutral solutes are listed in Table 1.[40] Several analytical-grade salts, i.e., NaCl, $MgCl_2$, $MgSO_4$, and Na_2SO_4 (Merck, Germany) were used to characterize the charge properties of the membranes. Glutathione ($C_{10}H_{17}N_3O_6S$, MW: 307.33, white powder) was purchased from Sigma-Aldrich. All chemicals were used as received.

Preparation of Torlon® PAI NF hollow fiber membranes

The hollow fiber membranes were prepared by the dry-jet wet-spinning process. Torlon® polymer was first dried in a vacuum oven at 120°C overnight to remove moisture, and then dissolved in NMP. The mixture was stirred for 24 h to form a homogeneous polymer solution, which was then set aside for 2 days to eliminate air bubbles that may have been trapped in the solution. The dope solution and the bore fluid were fed into the annulus and the inner tube of the spinneret separately by two ISCO syringe pumps. After the dope and the bore fluid met at the tip of the spinneret, they passed through an air gap region before entering the coagulation (water) bath. Finally, the as-spun hollow fibers were collected by a take-up drum. The experimental setup and the spinneret are described in Schematics 1 and 2 of the Supporting Information material. The detailed spinning conditions for the Torlon® PAI NF hollow fiber membranes are listed in Table 2.

Elongational stretching with the aid of various take-up speeds was performed on the spinning line during dry-jet wet spinning. The elongational draw ratio φ is defined as the ratio of the cross sectional area of the dope flow channel in the spinneret to the solid cross-sectional area of the precipitated hollow fiber membrane as follows:

$$\varphi = \frac{(\mathrm{OD}^2 - \mathrm{ID}^2)_{\mathrm{Spinneret}}}{(\mathrm{OD}^2 - \mathrm{ID}^2)_{\mathrm{Hollow-fiber}}} \tag{12}$$

where OD and ID refer to the outer and inner diameters (IDs), respectively. After spinning, the as-spun hollow fiber membranes were rinsed in a clean water bath for 3 days to remove the residual solvent. The hollow fiber membranes were then divided into two groups for post-treatments. One group was dipped in a 30 wt % glycerol aqueous solution for 48 h and dried in air at ambient temperature to be used in the making of membrane modules. The soaking of membranes in a liquid pore stabilizer such as an aqueous glycerol solution is a standard post-treatment method in industry to prevent pores from closing during drying. The other group was subjected to solvent exchange by immersing the membranes in methanol three times for 30 min at a time, and then in *n*-hexane three times, also for 30 min per time under stirring. The purpose of the solvent exchange process is to lower the surface tension of the liquid present in the membranes pores to preserve the membrane pore morphology in the dry state.[43] Finally, these fibers were dried in air at ambient temperature for further characterizations by SEM, AFM, and polarized FTIR.

Table 2. Spinning Conditions of Torlon® PAI NF Hollow Fiber Membranes

Torlon® dope solution	(wt %)	Torlon®/NMP (26.0:74.0)
Dope flow rate	(ml/min)	6.0
Bore fluid composition	(wt %)	NMP/Water (90:10)
Bore fluid flow rate	(ml/min)	3.0
Air gap	(cm)	5
Take-up speed	(m/min)	A: 15.0, B: 32.6, C: 54.6
External coagulant		Tap water, 26 ± 1°C
Dope temperature	(°C)	26 ± 1
Bore fluid temperature	(°C)	26 ± 1
Room humidity	(%)	65–70
Dimension of spinneret	(mm)	i.d./o.d. (1.05/1.6)
Die length L of spinneret	(mm)	6.5

Characterization

The morphology of the hollow fiber membranes spun at different take-up speeds was observed by a scanning electron microscope (SEM JEOL JSM-5600LV) and a field emission scanning electron microscope (FESEM JEOL JSM-6700F). Before observation, the dried hollow fibers were immersed in liquid nitrogen, fractured, and then coated with platinum using a JEOL JFC-1300 Platinum coater.

The membrane surface topology was examined using a Nanoscope IIIa atomic force microscope (AFM) from Digital Instruments. For each membrane, an area of 500 nm × 500 nm was scanned at a rate of 1 Hz using the tapping mode. The analysis of AFM pictures was carried out as described elsewhere.[44,45] Various roughness parameters such as the mean roughness (R_a), root mean square Z values (R_{ms}), and maximum vertical distance between the highest and lowest data points (R_{max}) were used to quantify the differences between various membranes. The sizes of nodule aggregates in both the x- and y-directions were determined from the averages of at least 10 sections of several fibers.

Polarized FTIR spectra of the hollow fiber membranes were measured with a Bio-Rad UMA 500 IR microscope attached with a Bio-Rad FTS 3500 FT-IR main bench. The system is equipped with a liquid nitrogen-cooled MCT detector and a polarizer. Measurements were carried out using a retro-reflection mode. For each sample, the outer surface reflectance was observed both in parallel and perpendicular to the axis of the hollow fiber to study the molecular orientation near the membrane surface induced by elongational stretching.

The overall porosity ε of the hollow fiber membrane was calculated as

$$\varepsilon = \left(1 - \frac{\rho_{\text{fiber}}}{\rho_{\text{Torlon}}}\right) \times 100\% \tag{13}$$

where ρ_{Torlon} is the density of the Torlon® powder, 1.38 g/cm^3.[46] The density of the hollow fiber membrane ρ_{fiber} was determined by Eq. 14, where the bulk volume V was obtained by measuring the inner and outer diameters (ODs) of the membrane under a microscope. The membrane weight m was measured on a digital balance.

$$\rho_{\text{fiber}} = \frac{m}{V} \tag{14}$$

To characterize the membrane surface charge characteristics, streaming potential measurements of Torlon® PAI flat membranes were performed with a SurPASS electrokinetic analyzer (Anton Paar GmbH, Austria). Torlon® PAI flat membranes were prepared by casting the polymer solution (with the same concentration as used for the spinning of the hollow fibers) on a glass plate by a blade with a 60 μm gap. Then, the as-cast membranes were immediately immersed into water. The zeta potential of a membrane was determined from the streaming potential along its surface.[47] A 0.01 M NaCl solution was circulated through the measuring cell containing the membrane sample. The relative movement of the charges in the electrochemical double layer gave rise to the streaming potential, which was detected by Ag/AgCl electrodes placed at both ends of the membrane sample. The electrolyte solution conductivity, temperature, and pH value were measured simultaneously. The classic Helmholtz-Schmoluchowski equation was applied without correction to calculate the apparent zeta potential.[48] Manual titration with 0.1 M HCl and 0.1 M NaOH was carried out to study the pH dependence of the zeta potential and thus determine the isoelectrical point (IEP).

Nanofiltration experiments with Torlon® PAI NF hollow fiber membranes

Nanofiltration experiments were conducted in a lab-scale circulating filtration unit, described previously.[49] Two modules for each hollow fiber sample were tested in the nanofiltration experiments, wherein each module comprised 10 fibers with an effective length of around 17 cm. Since the outer surface of the hollow fibers was the selective layer, the feed solution was pumped into the shell side, while the permeate solution exited from the lumen side of the hollow fibers. A high flow rate of 1.6 l/min was applied so that the effect of concentration polarization was minimized ($Re >$ 4000). Before testing, the hollow fiber membranes were conditioned at 12 bar for 0.5 h. Then, each membrane sample was subjected to the pure water permeation experiment at 10 bar to measure the PWP (l/m^2/bar/h), which was calculated using the equation

$$\text{PWP} = \frac{Q}{\Delta P \cdot A} \tag{15}$$

where Q is the water permeation volumetric flow rate (l/h), A is the effective filtration area (m^2), and ΔP is the transmembrane pressure drop (bar).

The mean effective pore size and the pore size distribution were obtained according to the protocol described below for the solute transport experiments. Different solutions containing neutral solutes, inorganic salts, and salt mixtures, were introduced to the membrane modules. The apparent solute separation coefficient R_T (%) was calculated using the equation:

$$R_T(\%) = \left(1 - \frac{c_p}{c_f}\right) \times 100 \tag{16}$$

where c_p and c_f are the solute concentration in the permeate and the feed solutions, respectively.

The procedures for the nanofiltration experiments were as follows:

1. Feed solutions were prepared by dissolving neutral solutes in deionized (DI) water at a concentration of about 200 ppm. The pressure difference across the membrane and the feed temperature were kept at 10 bar and 25°C, respectively, for all the experiments. The feed solutions were circulated for about 0.5 h until the system reached steady state. Both feed and permeate solutions were collected to measure the concentrations.
2. Nanofiltration experiments were conducted with neutral organic solutes of progressively higher molecular weights. Between runs of different solutes the membrane

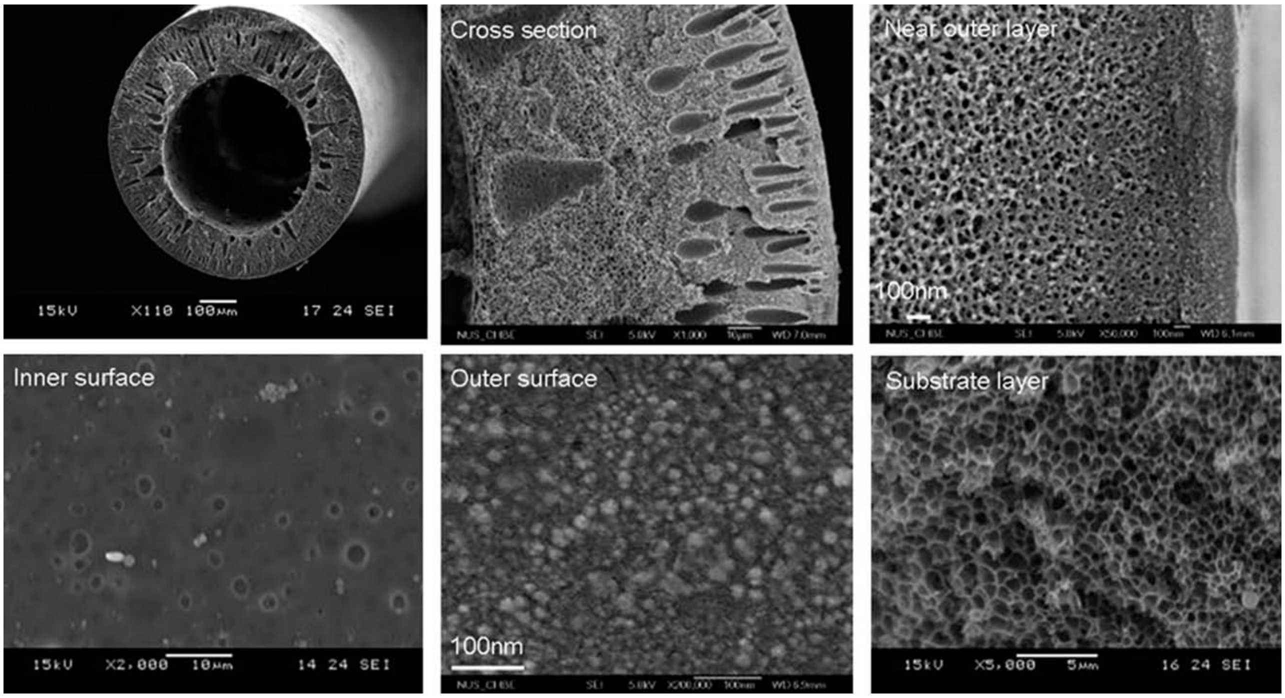

Figure 3. Morphology of Torlon® PAI NF hollow fiber membranes.

Take-up speed: 15 m/min.

was flushed thoroughly with DI water. The solute separation data were further used for the estimation of mean pore size and pore size distribution of the membrane.

3. NaCl solutions of different concentrations were prepared. The ion rejection by membranes was measured at different pressures to characterize the effective charge density of the membranes.

4. Different electrolyte solutions were prepared by dissolving single salts in DI water at a concentration 0.01 mol/l. The same experimental procedures as described in the Step (1) were used to measure salt rejection.

5. Binary NaCl/Na_2SO_4 salt solutions with different concentration ratios were prepared to test the ion fractionation performance of the membranes.

6. Glutathione solutions (200 ppm) were prepared by dissolving glutathione powder in DI water. NaOH (1.0 M) and HCl (1.0 M) solutions were used to modify the pH of the feed solutions; the solute rejection experiments were performed following the procedures of Step (1) with pH values between 3.3 and 8.8.

Concentrations of the neutral solute solutions were measured with a total organic carbon analyzer (TOC ASI-5000A, Shimazu, Japan), while those of single electrolyte solutions were measured with an electric conductivity meter (Schott Instruments, Lab 960, Germany). Concentrations of different ions in electrolyte mixtures were measured by ion chromatography (Metrohm, 792 Basic, Switzerland). The solution pH was determined using a pH meter (Horiba pH meter D-54, Japan).

Results and Discussion

Effects of take-up speed on membrane morphology, elongational draw ratio, and porosity

The typical morphology of Torlon® hollow fiber membranes is shown in Figure 3. The asymmetric membrane

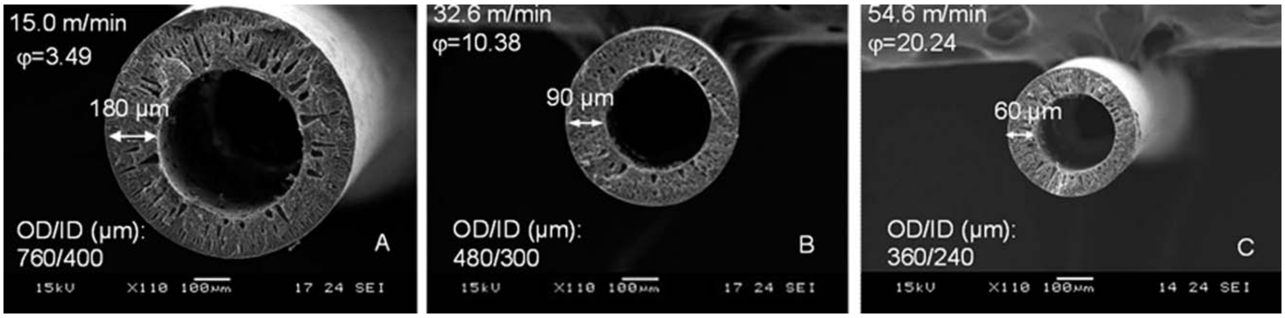

Figure 4. Effects of take-up speed on the membrane structure of Torlon® PAI NF hollow-fiber membranes.

The values at the left upper corner are the take-up speed and corresponding elongational draw ratio. The values at the left lower corner are the OD and ID of the hollow fiber membranes.

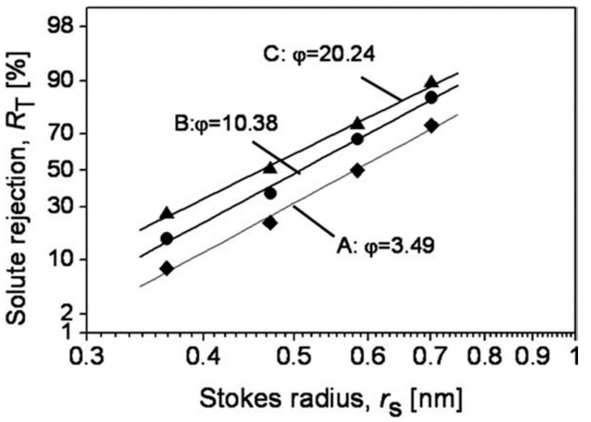

Figure 5. Log-normal probability plots of the effective rejection curves (solute rejections vs. their Stokes radii) for Torlon® PAI NF hollow fibers spun at different take-up speeds.

Table 3. Molecular Weight Cutoff, Mean Effective Pore Size (r_p), Geometric Standard Deviation (σ_p), and Pure Water Permeability of Torlon® PAI NF Hollow Fiber Membranes Spun at Different Take-up Speeds

Fiber	Draw Ratio φ	MWCO (Da)	r_p (nm)	σ_p	PWP (l/m^2/bar/h)
A	3.49	1538	0.58	1.37	2.77
B	10.38	1126	0.51	1.38	3.52
C	20.24	976	0.46	1.42	5.39

structure consists of an outer-selective skin, finger-like macrovoids, a sponge-like substructure, and a porous inner skin. The macrovoids are all oriented outwards, indicating that they possibly originate from external water induced intrusion during the phase inversion process.[50] The dimensions of the hollow fibers were affected by the take-up speed as illustrated in Figure 4. Both the OD and ID decrease with an increase in take-up speed, with the OD decreasing more significantly than the ID, resulting in a decrease in wall thickness with increasing elongational draw ratio. The overall porosities of the hollow fiber membranes spun at take-up speeds of 15.0, 32.6, and 54.6 m/min were 69%, 58%, and 53%, respectively. The reduction in overall porosities indicates the suppression of macrovoid formation with an increase in take-up speed, which was discussed extensively in our previous reports.[22,51]

Effects of take-up speed on mean pore size, pore size distribution, and pure water permeability

The newly developed Torlon® PAI NF hollow fiber membranes were characterized by the solute transport method described in Theoretical background to obtain the mean effective pore size and pore size distribution. The relationship between solute rejection and solute Stokes radius is shown on the log-normal probability graph in Figure 5. Linear relationships are obtained with reasonably high correlation coefficients ($r^2 > 0.95$). The mean effective pore radius μ_p at $R_T = 50\%$, the molecular weight cutoff (MWCO, the molecular weight of solute at $R_T = 90\%$) and the geometric standard deviation σ_p calculated from the plots are listed in Table 3. The pure water permeabilities, which were obtained from Eq. 15, of the hollow fiber membranes spun at different take-up speeds, are also listed in Table 3. The cumulative pore size distribution curves and probability density function curves of the PAI hollow fiber membranes calculated from Eqs. 1 and 3 are depicted in Figures 6a,b, respectively. It can be observed that the pore size distribution shifts towards left and becomes narrower with an increase in take-up speed.

Interestingly, from Table 3, it is noted that the PWP increases, whereas MWCO and the mean effective pore radius decreases, when the take-up speed is increased at the same dope flow rate, which has seldom been reported.[20] Key membrane properties that affect the rejection of organic molecules are MWCO, pore size, and membrane morphology.[52] However, the PWP is dependant on pore size, surface porosity, selective layer thickness, and tortuosity.[53,54] In this section, the effects of these parameters on the sieving property and PWP will be discussed.

The surface morphologies of the hollow fibers spun under different take-up speeds are shown in the AFM phase images in Figure 7 (the scan size is 500 × 500 nm), where the yellow sites represent the nodules whereas the dark sites are either the pores between the nodules or the nodules of lower heights. Interestingly, at the lowest take-up speed of 15.0 m/min, the phase image shows parallel stripes of higher and lower regions oriented perpendicular to the spinning direction. This surface morphology may be a result of rapid

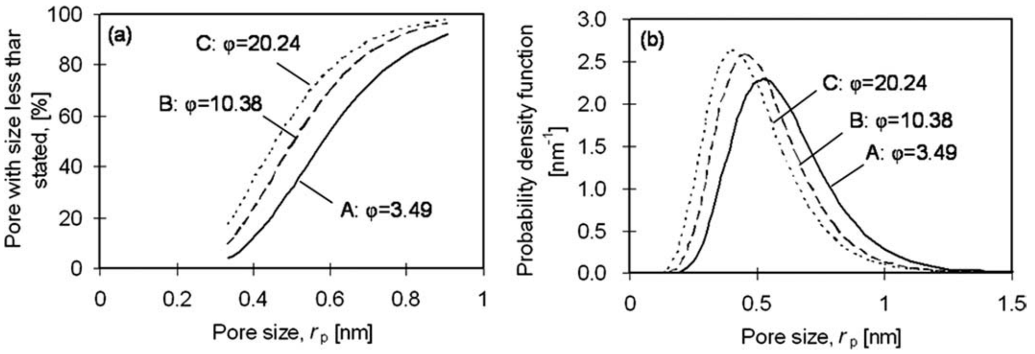

Figure 6. (a) Cumulative pore size distribution curves and (b) probability density function curves of the Torlon® PAI NF hollow-fiber membranes spun at different take-up speeds.

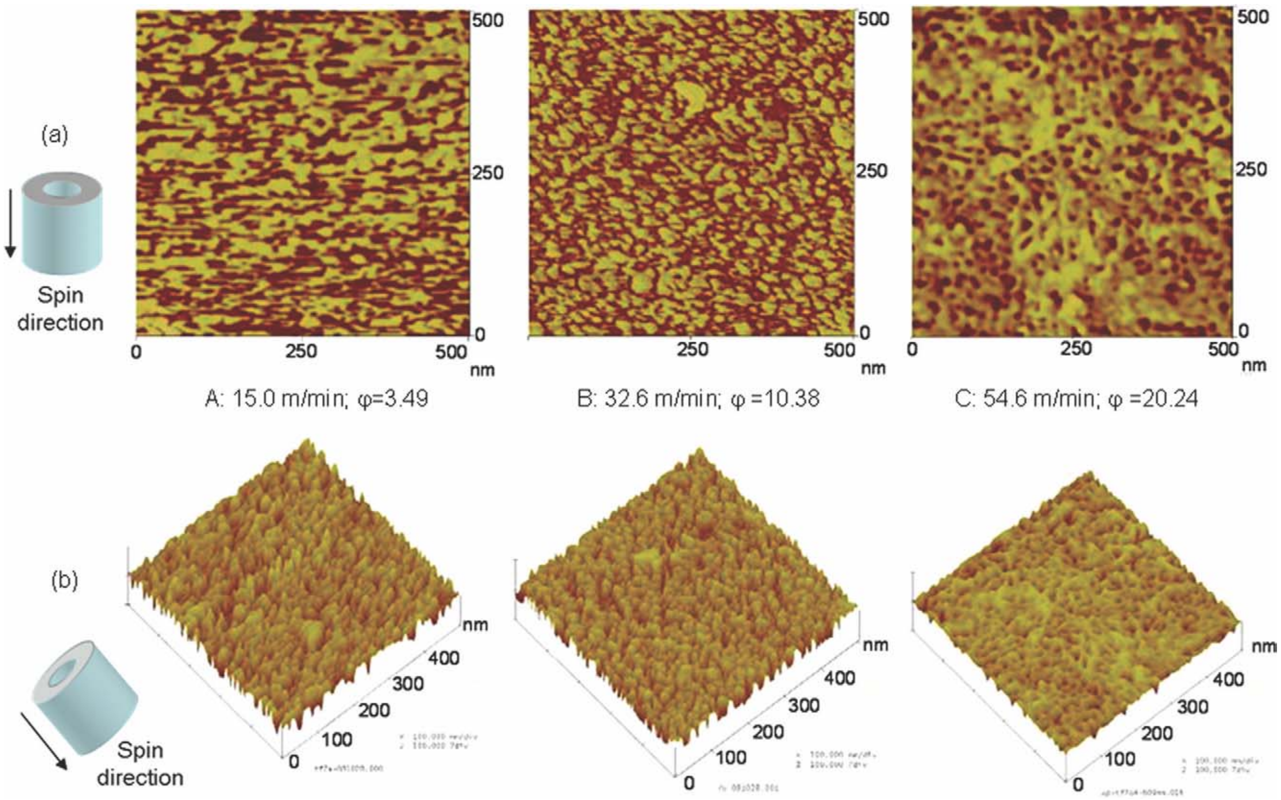

A: 15.0 m/min; φ=3.49

B: 32.6 m/min; φ =10.38

C: 54.6 m/min; φ =20.24

Figure 7. AFM images of the outer surface of Torlon® PAI NF hollow fiber spun at different take-up speeds.

(a) Phase image, (b) 3D image. [Color figure can be viewed in the online issue, which is available at www.interscience.wiley.com.]

solvent exchange, precipitation, and solidification when the hollow fiber enters the coagulation bath, with the significant solvent outflow causing the membrane surface to wrinkle. The stripe pattern disappears and a surface uniformly covered with nodules and valleys is formed at a higher take-speed of 32.6 m/min. The effects of elongational stretch become more profound at the highest take-up speed of 54.6 m/min, at which smaller pores intertwined with woven/fiber-like structure are formed in the surface layer, implying a severe segregation and stretch of nodules under elongational drawing. We have previously reported a similar structure induced by gravity at a higher air gap distance.[55]

One possible mechanism for the nano-pore morphological evolution is due to ‘‘nucleation and growth’’ and ‘‘spinodal phase separation,’’ as described in Figure 8. At low take-up speeds, the flux ratio of in-flow coagulant to out-flow solvent is low. As a result, the nascent fiber follows path (a) where ‘‘nucleation and growth’’ is the prevailing mechanism. The resultant fiber surface has a nodule-like surface layer, as observed in Figures 7A, B. A similar structure induced by shear rate within the spinneret can be found in our previous study.[45] When the take-up speed is further increased, path (b) becomes dominant. With the higher flux ratio of in-flow coagulant to out-flow solvent, the nascent hollow fiber rapidly traverses the binodal curve and enters the unstable region where ‘‘spinodal phase separation’’ takes place,[56] leading to a woven/fiber-like porous structure shown in Figure 7C. Both ‘‘nucleation and growth’’ and ‘‘spinodal phase separation’’ take place in path (b), but a high take-up speed or draw ratio facilitates the spinodal decomposition and forms a woven/fiber-like porous structure.[55]

A second possible mechanism is that of polymer chain disentanglement and energy dissipation. To further elaborate these phenomena, the membrane morphology was analyzed in terms of the roughness parameters R_a, R_{ms}, R_{max}, and the

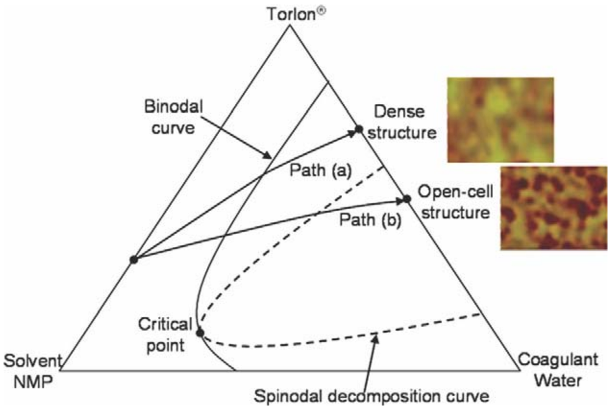

Figure 8. Phase diagram for a ternary system and the coagulation path during the precipitation of a Torlon® PAI hollow fiber at a constant temperature.

Path (a): nucleation and growth; Path (b): spinodal decomposition. [Color figure can be viewed in the online issue, which is available at www.interscience.wiley.com.]

Table 4. Effects of Take-up Speed on Roughness and Nodule Size of the Outer Surface of Torlon® PAI NF Hollow Fiber Membranes

Fiber ID	R_a (nm)	R_{ms} (nm)	R_{max} (nm)	Dimension of Nodules in x-Direction (nm)	Dimension of Nodules in y-Direction (nm)
A	0.72 (0.12)	0.93 (0.15)	10.71 (1.50)	72.5 (5.1)	70.6 (5.0)
B	1.41 (0.25)	1.74 (0.17)	14.33 (1.87)	50.9 (4.5)	50.9 (4.7)
C	1.55 (0.21)	1.97 (0.14)	16.30 (1.65)	35.2 (5.5)	35.2 (4.2)

R_a, mean roughness; R_{ms}, root mean square of Z values; R_{max}, maximum vertical distance between the highest and lowest data points. The values in the brackets are standard deviation. y-direction is the spinning direction

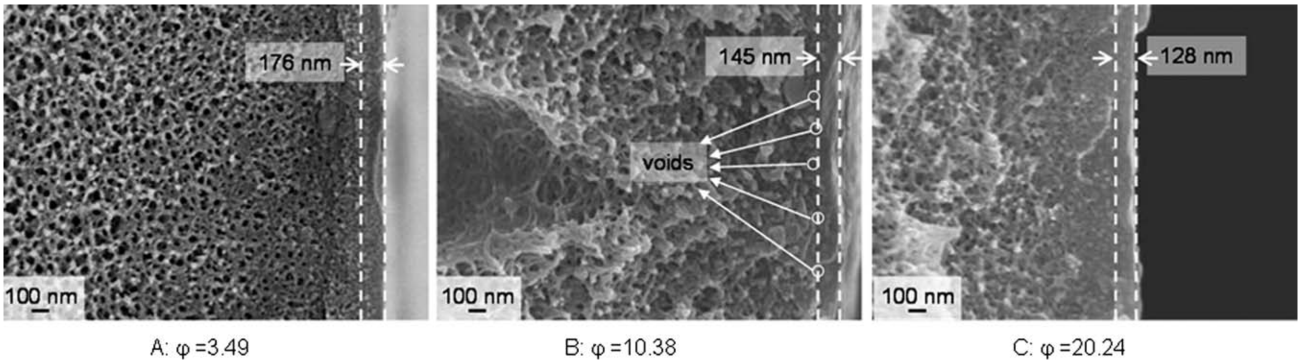

A: φ =3.49 B: φ =10.38 C: φ =20.24

Figure 9. FESEM images of the near outer layer of Torlon® PAI NF hollow fiber membranes spun at different take-up speeds.

nodule dimensions in the x and y directions. As shown in Table 4, the nodule sizes in both directions decreased while the roughness parameters increased with increases in take-up speed. It is believed that the nodular structure arises from rapid demixing of the polymer solution, followed by rapid vitrification.[45,55,56] Since the Torlon®/NMP spinning solutions exhibits shear-thinning and strain-thinning rheological behavior,[30] it can be concluded that Torlon® molecular chains will stretch, disentangle, and slide over one another during spinning at high elongational draw ratios. The disentangled and aligned polymer chains may result in smaller nodule sizes because of shorter-range interactions with

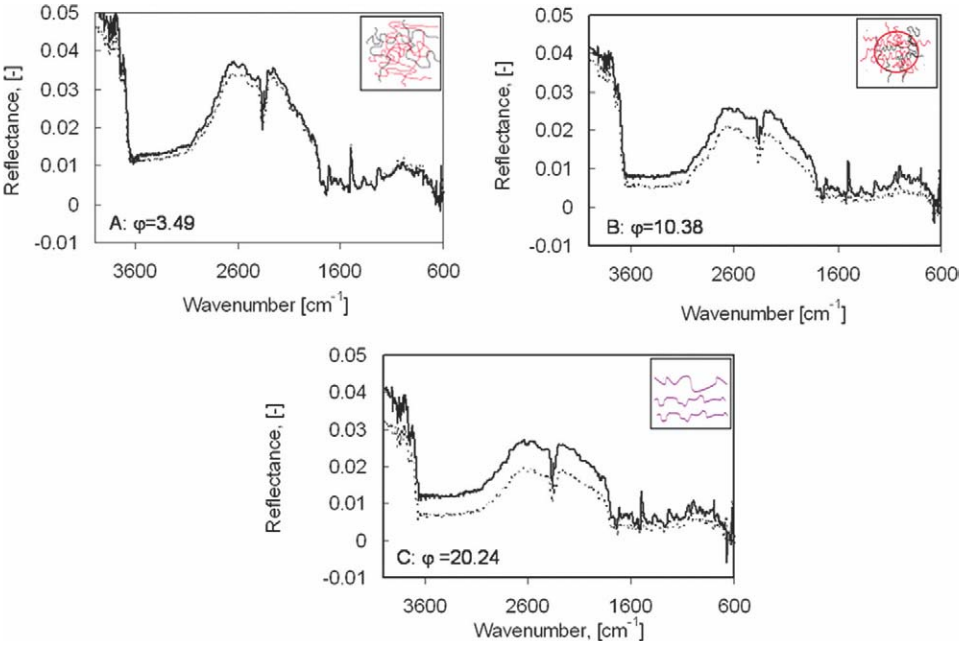

Figure 10. Polarized FTIR spectra of Torlon® PAI NF hollow fiber membranes.

Solid line: Parallel to spinning direction; Broken line: Perpendicular to spinning direction. The inset images are the proposed structures of polymer molecules near the surface. [Color figure can be viewed in the online issue, which is available at www.interscience.wiley.com.]

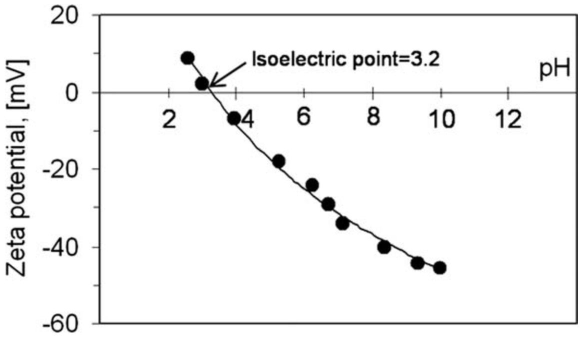

Figure 11. Zeta potential of Torlon® NF membrane as a function of pH.

Experiments were carried out with 0.01 M NaCl.

surrounding molecules compared to those of the unstretched and entangled chains. The smaller nodule size results in a smaller surface pore size due to easier and higher density packing of the nodules (see Figure 7), whereas the shorter-range interaction reduces the skin selective-layer thickness (see Figure 9) due to fewer chain entanglements with surrounding molecules. The smaller pores sizes ensure a higher solute rejection coefficient, while the thinner selective layer with reduced transport resistance allows for enhanced solvent fluxes. In addition, the high draw ratio may not only stretch the nascent nodules to form elongated fibers but also deform and elongate the pores beneath the skin surface to give narrower openings for enhanced solute rejection. The surface morphology shown in Figure 7C is a combined result of rapid phase inversion and high elongational drawing; the nano-size pores for separation may be located immediately underneath the skin surface.

To further verify the enhancement of molecular orientation in the skin layer with higher draw ratio, the membranes were characterized by polarized FTIR, which can detect directional inhomogeneities within a thin surface layer with a depth of less than ~150 nm.[57] The selective layer thicknesses of all membranes that we developed are close to or below this limit, as shown in the FESEM images in Figure 9. The FTIR spectra are shown in Figure 10. The solid lines represent the spectra measured with the polarization parallel to the spinning direction, while the broken lines represent the spectra with perpendicular polarization. There was only a small difference in reflectance between the parallel and perpendicular polarizations measured for the membranes spun at a low take-up speed. With increasing take-up speed, however, the difference becomes larger, indicating that a perpendicularly oriented skin was formed on the PAI hollow fiber membrane. These results indirectly confirm a significant difference in macromolecular stretch and orientation induced by the elongation stress during hollow fiber spinning that may create fiber-like nodules and elongated pores with enhanced rejection.

Membrane characterization using single electrolyte solutions

The charge characteristics of Torlon® PAI NF membranes were studied in terms of zeta potential, reflection coefficient, effective charge density, and rejection of single electrolyte solutions. As shown in Figure 11, the Torlon® PAI membrane has a slightly positive zeta potential below the isoelectric point of approximately pH 3.2, and is negatively charged above pH 3.2. This type of zeta potential curve is the characteristic of amphoteric surfaces consisting of carboxyl and amine functional groups on the membrane surface, in accordance with the molecular structure of Torlon® PAI illustrated in Figure 1. Therefore, the protonation of the amine functional groups leads to a positive surface charge below the isoelectric point, while the de-protonation of the carboxyl groups results in a negative charge above the isoelectric point.[58]

The reflection coefficient and charge density of the PAI hollow fiber membranes were determined from the transport and separation of NaCl at different pressures, and at different concentrations ranging from 1.0 to 50.0 mM. The Spiegler-Kedem model as written in Eq. 8, was regressed on the real rejection data as shown in Figure 12 to yield the membrane parameters σ and P/δ listed in Table 5. The Teorell-Meyer-Sievers model as written in Eqs. 9 and 11 was used to estimate the effective charge density (ΦX) of the NF membranes from σ at different NaCl concentrations, as shown in Figure 13. It is clear that the membranes with smaller pore sizes have a higher rejection and a higher effective charge density than those with larger pore sizes. Interestingly, for each membrane the rejection decreased (Figure 12) while the effective charge density increased (Figure 13) with an

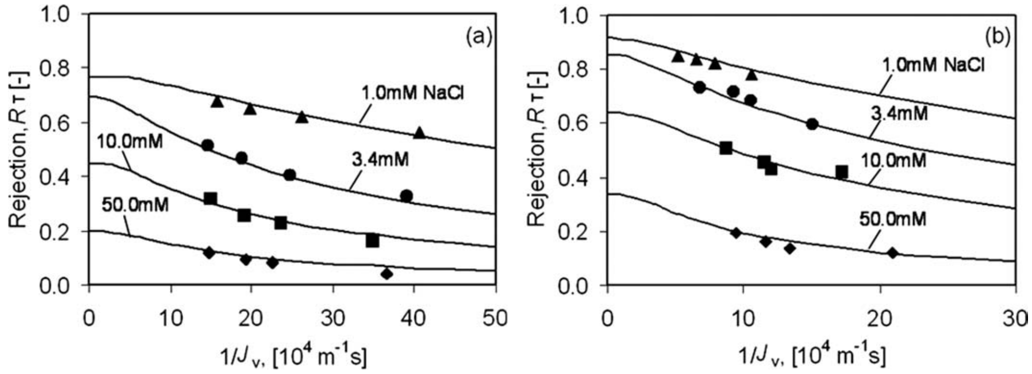

Figure 12. Rejections as function of permeate volume flux J_v with different NaCl concentrations.

(a) Membrane A with $r_p = 0.58$ nm; (b) Membrane C with $r_p = 0.46$ nm. The curves are fitted by the Spiegler-Kedem equations.

Table 5. Reflection Coefficient and Permeability of Various Concentrations of NaCl Determined from the Spiegler–Kedem Equations

Membrane ID	A		C	
NaCl (mM)	Reflection Coefficient, σ	Solute Permeability, P/δ ($\times 10^{-2}$ m/s)	Reflection Coefficient, σ	Solute Permeability, P/δ ($\times 10^{-2}$ m/s)
1.0	0.857	0.72	0.898	0.66
3.4	0.692	1.19	0.850	1.11
10.0	0.435	1.62	0.550	1.19
50.0	0.201	2.40	0.363	4.64

increase in electrolyte concentration. This is due to the reduction of the electrical double layer thickness within the pores with increases in the concentration of the electrolyte.[59]

Because the NF membranes are negatively charged at pH 5.75, they show different rejections for anions and cations with different valences. At the same molar concentration (0.01 mol/l), the rejections of four kinds of electrolytes measured at different pressures, as shown in Figure 14, decrease in the order $R(Na_2SO_4) > R(MgSO_4) > R(NaCl) > R(MgCl_2)$. In other words, the membranes show a higher rejection of divalent anions with higher co-ion charge than monovalent anions, and a lower rejection of divalent cations with higher counter-ion charge, corresponding to Donnan exclusion principle.[60] A slight deviation is the higher rejection of $MgSO_4$ than NaCl. According to Donnan exclusion, the rejection of these symmetric electrolytes should be equal. This deviation is due to the larger hydrated radii and smaller diffusivities of the Mg^{2+} and SO_4^{2-} ions than those of Na^+ and Cl^-.[61] It can also be observed from Figure 14 that the solute rejection increases with increasing pressures. This is due to the fact that the water permeate flux through the membrane is related linearly to the applied pressure difference, whereas the solute flux is dependent on several factors such as the concentration gradient over the membrane, the interaction between solute and fluid, and the water permeate flux. As a result, with increasing pressure difference, the water flux increases relatively faster than does the solute flux, which causes a decrease in solute permeate concentration and an increase in solute rejection.

Ion fractionation by Torlon® PAI NF membranes in the electrolyte mixture solutions

Generally, most electrolyte solutions may contain several salts that need to be separated through the membrane process. In this section, a standard binary salt mixture containing Na_2SO_4 and NaCl was used to test the ion fractionation performance of the as-spun PAI NF membrane. The concentration of Na_2SO_4 was kept at 0.01 mol/l while NaCl was added in increments to the system to change the concentration stepwise from 0.005 mol/l to 0.04 mol/l. As shown in Figure 15, more than 90% of Na_2SO_4 was rejected by the membrane while a negative rejection of NaCl at a low concentration was observed. This is due to the fact that Cl^- ions are forced to permeate preferentially compared to SO_4^{2-} ions since Cl^- has a lower valence, higher diffusivity, and smaller hydrated radius.[62] Na^+ ions also permeate together with Cl^- to maintain electroneutrality on both sides of the membrane, in accordance with the Donnan exclusion predictions.[60] At higher Cl^- concentrations, the priority of Cl^- over SO_4^{2-} to permeate the membrane was lowered, thus increasing the rejection of Cl^- and decreasing the rejection of SO_4^{2-}. The results shown in Figure 15 indicate that at a high concentration ratio of SO_4^{2-} to Cl^-, these two ions could be effectively fractionated by the negatively charged Torlon® PAI NF membranes.

Glutathione separation by Torlon® PAI NF hollow fiber membranes

As an amphoteric electrolyte molecule, in aqueous solution glutathione acts as both base (proton acceptor) and acid (proton donor), given that glutathione molecules includes amino ($-NH_2$), carboxyl ($-COOH$), and thiol ($-SH$) groups. As illustrated in Figure 2, glutathione is positively charged below pH 2.12 and negatively charged above pH 3.59. Within the range of $2.12 < pH < 3.59$, the molecule becomes net neutral. On the basis of the dissociation constants (pK_a values) of the amino groups in glutathione, the fraction of different ionization states at different pH values can be expressed by the following Henderson-Hasselbalch equation[63] plotted in Figure 16 (light broken curves):

$$\mathrm{pH} = \mathrm{p}K_a + \log\left(\frac{[\text{proton acceptor}]}{[\text{proton donor}]}\right) \tag{17}$$

Because Torlon® PAI NF membranes are also negatively charged at pH > 3.2 as shown in Figure 11, glutathione can be rejected by the NF membranes over a wide range of pH.

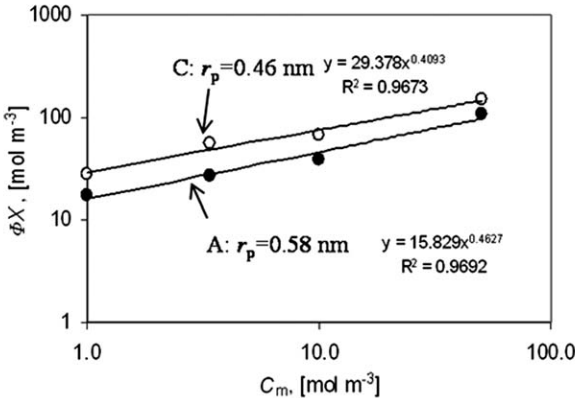

Figure 13. The effective charge density as a function of bulk NaCl molar concentration.

The curves are fitted according to Eq. 11.

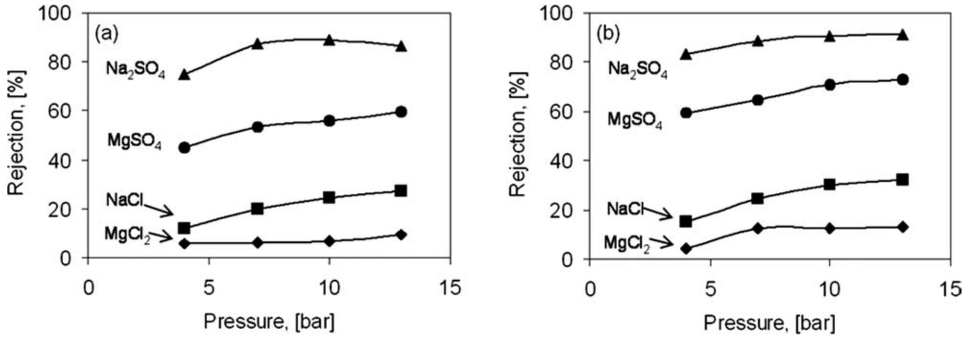

Figure 14. The rejection of different salts at different pressures.

(a) Membrane A with $r_p = 0.58$ nm; (b) Membrane C with $r_p = 0.46$ nm. (The bulk solution concentration: 0.01 mol/l, pH 5.75).

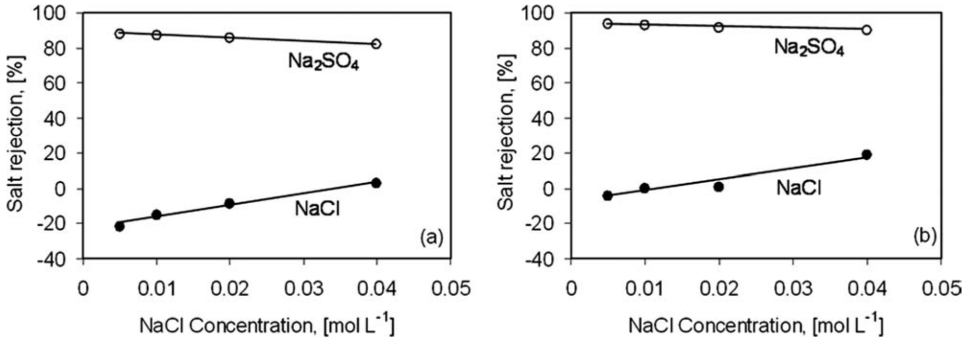

Figure 15. Salt rejection of the binary mixture of NaCl/Na$_2$SO$_4$ solution as a function of NaCl concentration.

(a) Membrane A with $r_p = 0.58$ nm; (b) Membrane C with $r_p = 0.46$ nm. (Na$_2$SO$_4$ concentration was kept at 0.01 mol/l, pH 5.75).

Nanofiltration rejection of glutathione by membrane C with $r_p = 0.46$ nm was measured at a pressure of 10 bar. As illustrated in Figure 16, more than 99.5% glutathione is rejected above pH 4.5. At pH values around the pI (2.12–3.59), the rejection of glutathione (~57.1%) is slightly higher than that of saccharose (~50.6%), which has almost the same molecular weight as glutathione. These results confirm that solution pH has the dominant effect on the separation of glutathione because pH determines the ionization states of the glutathione molecules and surface charge characteristics of the PAI membranes. The rejection of glutathione is also dependent on the pore size (steric exclusion) and the electrostatic interaction between solutes and membrane.

Conclusions

A novel Torlon® polyamide-imide nanofiltration hollow fiber membrane was developed using the dry-jet wet-spinning process. We found that the external stretching had a great influence on membrane structure, nano-pore formation, and nanofiltration performance. AFM images demonstrate that a high take-up speed favors the ''spinodal decomposition'' rather than the ''nucleation and growth'' mechanism, which increases surface porosity, and thus, increases PWP. Polarized FTIR verified that the molecular orientation was perpendicular to the spinning direction. The pore size and the MWCO decreased while the PWP increased with an increase in take-up speed. Therefore, this study demonstrates that high take-up speed spinning improves not only the productivity of hollow fibers, but also the solute rejection and the water permeability, which may become a meaningful instructive guideline in the fabrication of high performance hollow fiber membranes. The Torlon® PAI hollow fiber membrane spun at 54.6 m/min has a mean pore radius of 0.46 nm and a narrow pore size distribution. The PWP was achieved at 5.39 l/m/bar/h.

The Torlon® PAI NF membranes show the highest rejection of divalent anions, a lower rejection of monovalent ions, and the lowest rejection of divalent cations, which is in

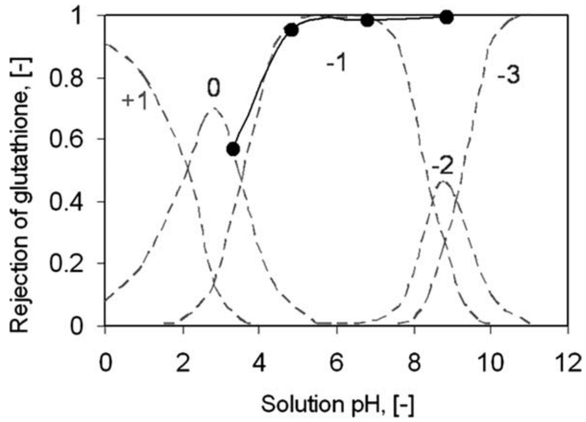

Figure 16. The rejection of glutathione (200 ppm) as affected by the solution pH by membrane C with $r_p = 0.46$ nm.

accordance with the Donnan exclusion principle. Zeta-potential measurements indicate that the isoelectric point of Torlon® PAI membrane is 3.2, above which the membrane is negatively charged. With a binary NaCl/Na_2SO_4 solution, a negative rejection of Cl^- and a high rejection of SO_4^{2-} were observed indicating the potential use of these membranes for the fractionation of salt mixtures.

A greater than 99.5% rejection of glutathione molecules was obtained using the newly-developed Torlon® PAI NF hollow fiber membrane on appropriate adjustment of the feed solution pH. Therefore, based on the interaction between the charged membrane surface and the ionized glutathione molecules under different pH conditions, these new membranes hold great potential for the effective recovery, concentration, and purification of glutathione like molecules from aqueous solution containing lower molecular weight impurities.

Acknowledgments

The authors acknowledge the Singapore-MIT-Alliance (SMA) for research funding and Ph.D. scholarships for Mr. Sun Shipeng, and the National University of Singapore (NUS) for grants R-279-000-249-646 and R-279-000-271-272. Thanks are also due to Dr. Yang Qian, Dr. Teoh May May, Dr. Li Yi, Miss. Peng Na, Miss. Cheng Jiuhua, Miss. Natalia Widjojo, Miss. Wang Yan, and Miss. Low Bee Ting for their valuable comments and suggestions to this study.

Notation

A = effective filtration area of membrane (m^2)
c_f = solute concentration in the feed solution (mol/m^3)
c_m = concentration at the membrane surface (mol/m^3)
c_p = solute concentration in the permeate (mol/m^3)
D_i = diffusivity of ion i in free solution (m^2/s)
D_s = diffusivity of solute in the solution (m^2/s)
J_s = solute or ion flux ($mol/m^2/s$)
J_v = permeate flux ($m^3/m^2/s$)
MW = molecular weight (Da)
MWCO = molecular weight cutoff (Da)
OD = outer diameter (μm)
ID = inner diameter (μm)
P = Intrinsic solute permeability (m^2/s)
Δp = trans-membrane pressure drop (bar)
pK_a = ionization equilibrium constant (–)
PWP = pure water permeability ($l/m^2/bar/h$)
Q = water permeate flux (m^3/h)
r_s = solute Stokes radius (nm)
r_p = effective pore radius (nm)
R_T = solute rejection (–)
α = transport number of cations in free solution defined as $\alpha = D_1/(D_1 + D_2)$
δ = membrane thickness (m)
ε = overall porosity (–)
μ_p = mean effective pore radius (nm)
μ_s = geometric mean radius of solute at $R_T = 50\%$ (nm)
ξ = ratio of effective volume charge density (ΦX) of membrane to the electrolyte concentration (c_m) at the membrane surface
$\Delta\pi$ = osmotic pressure difference (bar)
σ = reflection coefficient (–)
σ_g = geometric standard deviation about μ_s (–)
σ_p = geometric standard deviation about μ_p (–)
ΦX = effective membrane charge (mol/m^3)

Literature Cited

1. Schäfer AI, Fane AG, Waite TD. *Nanofiltration: Principles and Applications*. Oxford, UK: Elsevier, 2002.
2. Van der Bruggen B, Vandecasteele C, Van Gestel T, Doyen W, Leysen R. A review of pressure-driven membrane processes in wastewater treatment and drinking water production. *Environ Prog*. 2003;22:46–56.
3. Sutherland K. Developments in filtration: What is nanofiltration? *Filtr Sep*. 2008;45:32–35.
4. Peng W, Escobar IC. Rejection efficiency of water quality parameters by reverse osmosis and nanofiltration membranes. *Environ Sci Technol*. 2003;37:4435–4441.
5. Shannon MA, Bohn PW, Elimelech M, Georgiadis JG, Marinas BJ, Mayes AM. Science and technology for water purification in the coming decades. *Nature*. 2008;452:301–310.
6. Shintani T, Matsuyama H, Kurata N, Ohara T. Development of a chlorine-resistant polyamide nanofiltration membrane and its field-test results. *J Appl Polym Sci*. 2007;106:4174–4179.
7. Van der Bruggen B, Manttari M, Nystrom M. Drawbacks of applying nanofiltration and how to avoid them: A review. *Sep Purif Technol*. 2008;63:251–263.
8. Sirkar KK. Application of membrane technologies in the pharmaceutical industry. *Curr Opin Drug Discov Devel*. 2000;3:714–722.
9. Wang XL, Ying AL, Wang WN. Nanofiltration of L-phenylalanine and L-aspartic acid aqueous solutions. *J Membr Sci*. 2002;196:59–67.
10. White LS. Development of large-scale applications in organic solvent nanofiltration and pervaporation for chemical and refining processes. *J Membr Sci*. 2006;286:26–35.
11. Petersen RJ. Composite reverse-osmosis and nanofiltration membranes. *J Membr Sci*. 1993;83:81–150.
12. Baker RW. *Membrane Technology and Applications*. West Sussex, England: John Wiley & Sons Ltd., 2004.
13. Wang KY, Chung TS. Fabrication of polybenzimidazole (PBI) nanofiltration hollow fiber membranes for removal of chromate. *J Membr Sci*. 2006;281:307–315.
14. Elhibri MJ, Paul DR. Effects of uniaxial drawing and heat-treatment on gas sorption and transport in PVC. *J Appl Polym Sci*. 1985; 30:3649–3678.
15. Shilton SJ, Bell G, Ferguson J. The rheology of fiber spinning and the properties of hollow-fiber membranes for gas separation. *Polymer*. 1994;35:5327–5335.
16. Chung TS, Lin WH, Vora RH. The effect of shear rates on gas separation performance of 6FDA-durene polyimide hollow fibers. *J Membr Sci*. 2000;167:55–66.
17. Niwa A, Kawakami H, Kanamori T, Shinbo T, Kaito A, Nagaoka S. Surface orientation effect of asymmetric polyimide hollow fibers on their gas transport properties. *J Membr Sci*. 2004;230:141–148.
18. Qin JJ, Gu J, Chung TS. Effect of wet and dry-jet wet spinning on the sheer-induced orientation during the formation of ultrafiltration hollow fiber membranes. *J Membr Sci*. 2001;182:57–75.
19. Chou WL, Yang MC. Effect of take-up speed on physical properties and permeation performance of cellulose acetate hollow fibers. *J Membr Sci*. 2005;250:259–267.
20. Wang KY, Chung TS. Polybenzimidazole nanofiltration hollow fiber for cephalexin separation. *AIChE J*. 2006;52:1363–1377.
21. Omole IC, Miller SJ, Koros WJ. Increased molecular weight of a cross-linkable polyimide for spinning plasticization resistant hollow fiber membranes. *Macromolecules*. 2008;41:6367–6375.
22. Wang KY, Li DF, Chung TS, Chen SB. The observation of elongation dependent macrovoid evolution in single and dual-layer asymmetric hollow fiber membranes. *Chem Eng Sci*. 2004;59:4657–4660.
23. Robertson GP, Guiver MD, Yoshikawa M, Brownstein S. Structural determination of Torlon (R) 4000T polyamide-imide by NMR spectroscopy. *Polymer*. 2004;45:1111–1117.
24. Wang Y, Jiang LY, Matsuura T, Chung TS, Goh SH. Investigation of the fundamental differences between polyamide-imide (PAI) and polyetherimide (PEI) membranes for isopropanol dehydration via pervaporation. *J Membr Sci*. 2008;318:217–226.
25. Yoshikawa M, Higuchi A, Ishikawa M, Guiver MD, Robertson GP. Vapor permeation of aqueous 2-propanol solutions through gelatin/Torlon((R)) poly(amide imide) blended membranes. *J Membr Sci*. 2004;243:89–95.
26. Higuchi A, Yoshikawa M, Guiver MD, Robertson GP. Vapor permeation and pervaporation of aqueous 2-propanol solutions through the Torlono (R) poly(amide imide) membrane. *Sep Sci Technol*. 2005; 40:2697–2707.

27. Teoh MM, Chung TS, Wang KY, Guiver MD. Exploring Torlon/P84 co-polyamide-imide blended hollow fibers and their chemical cross-linking modifications for pervaporation dehydration of isopropanol. *Sep Purif Technol.* 2008;61:404–413.
28. Peng N, Chung TS. The effects of spinneret dimension and hollow fiber dimension on gas separation performance of ultra-thin defect-free Torlon (R) hollow fiber membranes. *J Membr Sci.* 2008;310: 455–465.
29. Kosuri MR, Koros WJ. Defect-free asymmetric hollow fiber membranes from Torlon (R), a polyamide-imide polymer, for high-pressure CO2 separations. *J Membr Sci.* 2008;320:65–72.
30. Peng N, Chung T-S, Lai J-Y. The rheology of Torlon® solutions and its role in the formation of ultra-thin defect-free Torlon® hollow fiber membranes for gas separation. *J Membr Sci.* 2009;326:608–617.
31. Wijaya JE. *Formation and Characterization of Solvent Resistant Nanofiltration Membranes.* Master thiesis, University of Ottawa, 2005.
32. Sies H. Glutathione and its role in cellular functions. *Free Radic Biol Med.* 1999;27:916–921.
33. Sakato K, Tanaka H. Advanced control of glutahione fermentation process. *Biotechnol Bioeng.* 1992;40:904–912.
34. Gotoh T, Iguchi H, Kikuchi KC. Separation of glutathione and its related amino acids by nanofiltration. *Biochem Eng J.* 2004;19:165–170.
35. Van der Bruggen B, Schaep J, Wilms D, Vandecasteele C. A comparison of models to describe the maximal retention of organic molecules in nanofiltration. *Sep Sci Technol.* 2000;35:169–182.
36. Aimar P, Meireles M, Sanchez V. A contribution to the translation of retention curves into pore-size distributions for sieving membranes. *J Membr Sci.* 1990;54:321–338.
37. Bowen WR, Mohammad AW. Characterization and prediction of nanofiltration membrane performance: A general assessment. *Chem Eng Res Des.* 1998;76:885–893.
38. Kedem O, Katchalsky A. Thermodynamic analysis of the permeability of biological membranes to non-electrolytes. *Biochim Biophys Acta.* 1958;27:229–246.
39. Spiegler KS, Kedem O. Thermodynamics of hyperfiltration (reverse osmosis): Criteria for efficient membranes. *Desalination.* 1966;1: 311–326.
40. Wang XL, Tsuru T, Nakao S, Kimura S. The electrostatic and steric-hindrance model for the transport of charged solutes through nanofiltration membranes. *J Membr Sci.* 1997;135:19–32.
41. Newman JS. *Electrochemical Systems*, 2nd ed. NewJersey: Prentice Hall, 1991.
42. Wang KY, Chung TS. The characterization of flat composite nanofiltration membranes and their applications in the separation of Cephalexin. *J Membr Sci.* 2005;247:37–50.
43. Park HC, Moon YS, Rhee HW, Won J, Kang YS, Kim UY. Effect of solvent exchange on the morphology of asymmetric membranes. In: Pinnau I, Freeman BD, editors. *Membrane Formation and Modification.* Washington, DC: American Chemical Society, 2000: 110–124.
44. Khulbe KC, Matsuura T. Characterization of synthetic membranes by Raman spectroscopy, electron spin resonance, and atomic force microscopy; a review. *Polymer.* 2000;41:1917–1935.
45. Chung TS, Qin JJ, Huan A, Toh KC. Visualization of the effect of die shear rate on the outer surface morphology of ultrafiltration membranes by AFM. *J Membr Sci.* 2002;196:251–266.
46. Mark JE. *Polymer Data Handbook.* New York: Oxford University Press, 1999.
47. Childress AE, Elimelech M. Effect of solution chemistry on the surface charge of polymeric reverse osmosis and nanofiltration membranes. *J Membr Sci.* 1996;119:253–268.
48. Manttari M, Pihlajamaki A, Nystrom M. Effect of pH on hydrophilicity and charge and their effect on the filtration efficiency of NF membranes at different pH. *J Membr Sci.* 2006;280:311–320.
49. Wang KY, Matsuura T, Chung TS, Guo WF. The effects of flow angle and shear rate within the spinneret on the separation performance of poly (ethersulfone) (PES) ultrafiltration hollow fiber membranes. *J Membr Sci.* 2004;240:67–79.
50. Widjojo N, Chung TS. Thickness and air gap dependence of macrovoid evolution in phase-inversion asymmetric hollow fiber membranes. *Ind Eng Chem Res.* 2006;45:7618–7626.
51. Peng N, Chung TS, Wang KY. Macrovoid evolution and critical factors to form macrovoid-free hollow fiber membranes. *J Membr Sci.* 2008;318:363–372.
52. Bellona C, Drewes JE, Xu P, Amy G. Factors affecting the rejection of organic solutes during NF/RO treatment: A literature review. *Water Res.* 2004;38:2795–2809.
53. Kokubo K, Sakai K. Evaluation of dialysis membranes using a tortuous pore model. *AIChE J.* 1998;44:2607–2619.
54. Singh S, Khulbe KC, Matsuura T, Ramamurthy P. Membrane characterization by solute transport and atomic force microscopy. *J Membr Sci.* 1998;142:111–127.
55. Chung TS. The limitations of using Flory-Huggins equation for the states of solutions during asymmetric hollow-fiber formation. *J Membr Sci.* 1997;126:19–34.
56. Kim JY, Lee HK, Kim SC. Surface structure and phase separation mechanism of polysulfone membranes by atomic force microscopy. *J Membr Sci.* 1999;163:159–166.
57. Niwa M, Kawakami H, Kanamori T, Shinbo T, Kaito A, Nagaoka S. Gas separation of asymmetric 6FDA polyimide membrane with oriented surface skin layer. *Macromolecules.* 2001;34:9039–9044.
58. Childress AE, Elimelech M. Relating nanofiltration membrane performance to membrane charge (electrokinetic) characteristics. *Environ Sci Technol.* 2000;34:3710–3716.
59. Peeters JMM, Mulder MHV, Strathmann H. Streaming potential measurements as a characterization method for nanofiltration membranes. *Colloid Surf A Physicochem Eng Asp.* 1999;150:247–259.
60. Donnan FG. Theory of membrane equilibria and membrane potentials in the presence of non-dialysing electrolytes. *J Membr Sci.* 1995;100:45–55.
61. Schaep J, Van der Bruggen B, Vandecasteele C, Wilms D. Influence of ion size and charge in nanofiltration. *Sep Purif Technol.* 1998; 14:155–162.
62. Tanninen J, Manttari M, Nystrom M. Effect of salt mixture concentration on fractionation with NF membranes. *J Membr Sci.* 2006; 283:57–64.
63. Stryer L. *Biochemistry*, 4th ed. New York: Freeman, 1995.

Manuscript received Apr. 25, 2009, and revision received Aug. 17, 2009.